# LANGMUIR

pubs.acs.org/Langmuir Article

# Quasi-2D Model to Predict Solid Microstructure in Drying Thin Films

Jesse L. Starger, Aaron T. Fafarman, Jason B. Baxter, Nicolas J. Alvarez,\* and Richard A. Cairncross\*



Cite This: Langmuir 2023, 39, 16231-16243



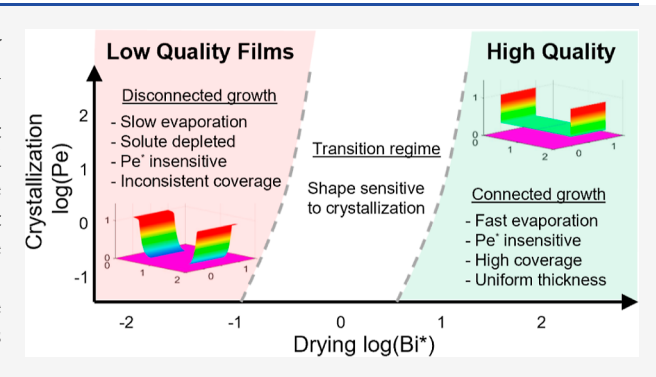
**ACCESS** I

Metrics & More

Article Recommendations

Supporting Information

**ABSTRACT:** The microstructure of solid coatings produced by solution processing is highly dependent on the coupling between growth, solute diffusion, and solvent evaporation. Here, a quasi-2D numerical model coupling drying and solidification is used to predict the transient lateral growth of two adjacent nuclei growing toward each other. Lateral gradients of the solute and solvent influence the evolution of film thickness and solid growth rate. The important process parameters and solvent properties are captured by the dimensionless Peclet number (Pe) and the Biot number (Bi), modified by an aspect ratio defined by the film thickness and distance between nuclei. By variation of Pe and Bi, the evaporation dynamics and aspect ratio are shown to largely determine the coating quality.



These findings are applied to drying thin films of crystallizing halide perovskites, demonstrating a convenient process map for capturing the relationship between the modified *Bi* and well-defined coating regimes, which may be generalized for any solution-processed thin film coating systems.

#### INTRODUCTION

Models relating solid microstructure to the kinetics of nucleation and growth have undergone minimal changes since the early works of LaMer, Avrami, Volmer, Weber, and others. <sup>1-6</sup> While these models provide qualitative insight into the growth rates of phase-change systems, their quantitative application is very limited. <sup>7,8</sup> Furthermore, the models were originally formulated for bulk phase change materials and therefore do not have the necessary physics to explain the growth rates in confined geometries, i.e., thin films. The lack of broad applicability makes the predictive selection of material and process conditions for high quality films from first-principles challenging.

As thin film technology grows in application, there is a need for physics-based film growth models that incorporate evaporation to predict the final film growth and morphology. For example, the past decade has seen a surge in research and development of solution-based processing schemes for perovskite thin film technologies. However, the complex interplay between the process parameters and the final film performance is not well understood. This lack of understanding has arguably hindered the successful implementation of film processing methods and resulted in costly trial and error methods to establish suitable process parameters and solute/solvent formulations. 10,11 It follows that large-area films made by continuous coating methods necessary for commercial implementation have lagged considerably behind the performances obtained in small-scale, batch-processed (especially spincoated) research samples.

A poorly coated film may be characterized by incomplete substrate coverage or an irregular thickness of the final dried film. Though much work has been done on the formation and microstructure of grain boundaries, quantitatively predicting large scale microstructure in drying and solidifying thin films remains an important challenge in enabling continuous coating strategies. 12,13 Predictive modeling in thin films typically begins by considering diffusion-driven growth in the bulk, i.e., Fick's first and second laws. However, treatment of these equations is usually local to the solid boundary, such that the transport of solute through the bulk fluid is effectively semi-infinite, thus neglecting the effects of confinement and solute depletion by nearest neighbors or transient solute concentration through evaporation.<sup>9,14</sup> Phase-change models, such as Avrami's equation, capture the macroscopic evolution of a system but do not account for multiple growth dimensions such as lateral and vertical growth. In a thin film, the wet film height will vary significantly with evaporation and, by definition, vertically confine the growing solid domain. The thin film confinement has been shown to affect growth rates in polymer systems such as isotactic polystyrene. 18 Without quantitative theories that accurately describe the general physics underlying evaporation and solidification in thin films, we lack fundamental relation-

Received: May 31, 2023 Revised: October 9, 2023 Accepted: October 9, 2023 Published: November 8, 2023





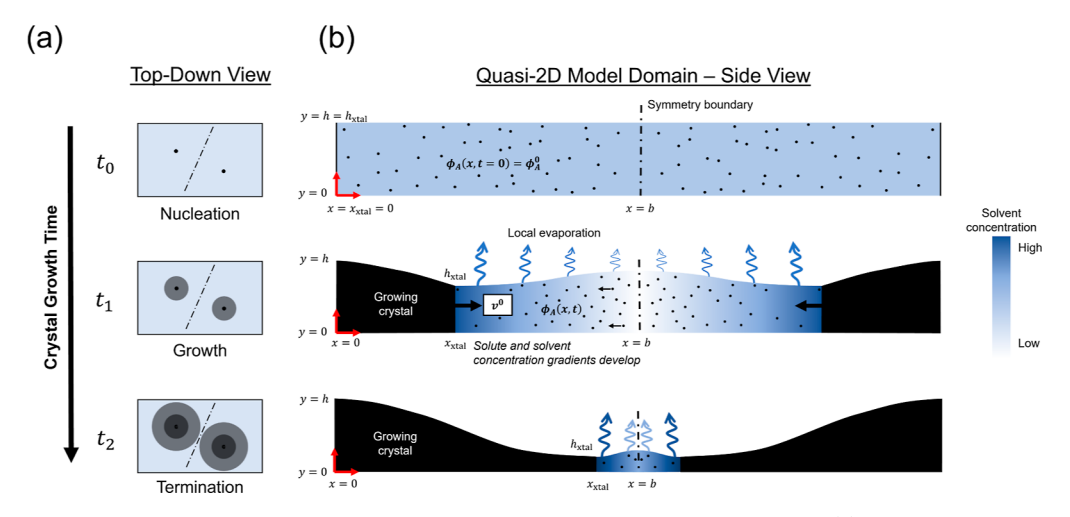


**Figure 1.** Schematic depicting relevant physics of coupled solidification and drying in a thin film. (a) A top-down representation of the solidification pathway in a thin film corresponding to nucleation (initial condition), growth, and termination. (b) A side view corresponding to the quasi-2D model formulated here, depicting the solid-liquid interface ( $x_{\text{xtal}}$ ) approaching the symmetry plane at ( $x_{\text{tal}} = b$ ).

ships by which to select materials and process parameters for the next generation of scalable thin film processing methods.

In this study, we introduce a novel quasi-2D transient model that couples growth kinetics, solute diffusion, solvent evaporation, and interdomain competition for solute. The model assumes that growth is governed by kinetics at the nucleated solid surface, while solute transport is regulated by 1D diffusion from the surrounding bulk. The model's quasi-2D nature arises from the explicit incorporation of the spatial variation of liquid film height into the diffusion equation, with the assumption that solute and solvent diffusion is vertically fast (thus the concentration only varies laterally and with time). More specifically, evaporation from the top of the film is a function of the solvent concentration distribution in solution, leading to nonuniform evaporative fluxes along the interface. Nonuniform evaporative fluxes result in variations in solute concentration that directly affect growth kinetics and the resulting solid's surface topography. To account for the moving solid front, the model employs a finite difference moving mesh routine. The model is formulated with two dimensionless parameters, a modified Bi and a Pe, which are used to predict the transient growth behavior, bulk conditions, and the resulting solid profile from a nucleated center. The results are presented in dimensionless form to generalize the results.

#### METHODS

Quasi-2D Physics of Solid Growth and Drying in a Thin Confined Volume. The schematic in Figure 1 underlines the important physics of the quasi-2D diffusion and evaporation model. Figure 1 at  $t_0$  displays the initial liquid film consisting of a binary mixture of solute and solvent confined by a solid surface at x = 0 that spans the height of the wet film and a symmetry plane in the bulk at x= b. Solute is treated as a single species with a single diffusion coefficient and the model ignores any effects due to electrostatics, intermediate species, or viscosity. However, the former effects are indirectly incorporated into the linear growth velocity  $(v_0)$  of the growing solid domain. In this way, the model is left as general as possible and agnostic to specific chemical pathways or intermediate species. The latter effect of viscosity directly affects the diffusion coefficient; however, the change in viscosity is assumed to be sufficiently small with time that changes in the solute diffusion coefficient can be ignored. At the solidifying boundary  $x_{\text{xtal}}(t)$  (initially at x = 0) with height  $y = h_{xtal}$ , solute transfers from the liquid side of the boundary to the solid side at a rate that is assumed to be governed

by first-order kinetics, i.e., proportional to the degree of supersaturation. A concentration gradient in solvent and solute arises from the depletion of solute at the solidifying boundary, which drives the diffusion of solute from the bulk liquid toward  $x_{\rm xtal}$ . Simultaneously, solvent is removed in the *y*-direction vertically by evaporation through the top of the film at a rate proportional to the local solvent concentration. As solidification and drying proceed, the location of the solidifying interface advances toward the far boundary of the domain, i.e.,  $x_{\rm xtal}(t \to \infty) = b$ . The model assumes that only solvent evaporates and that the evaporation rate is calculated along the film position as a function of the local solvent concentration, such that the wet film height is allowed to vary with position x, i.e., h(x, t).

We also neglect convective effects due to gradients that may develop in height, surface tension (Marangoni and "coffee ring"), or temperature (Rayleigh–Benard).  $^{16,17}$  These assumptions are reasonable for sufficiently thin films where the evaporation rate is such that instabilities cannot develop appreciably and for steady-state coatings (such as roll-to-roll) where dewetting is avoided. This assumption is justified experimentally by Ahmadian-Yazdi and Eslamian, who have shown that in the context of perovskite films thinner than 80  $\mu \rm m$  Marangoni type instabilities can be ignored.  $^{18}$  Thus, the model and discussion in this work are restricted to thin films that remain stable during the drying process.

We assume that all concentration gradients in the y-direction are zero, i.e., the diffusion in the y-direction is very fast compared to evaporation. This assumption is justified by calculating the mass transfer Bi ( $Bi = \tau_{D,y}/\tau_{evap} = H\overline{\beta}/D$ ), where D is the diffusion coefficient, H is the wet-film thickness, and  $\bar{\beta}$  is the average evaporation velocity. The transient solution for vertical diffusion (leading to vertical concentration gradients) is typically ignored when  $Bi \ll 1$ , which is the case for many common volatile solvents used in thin film coatings (see Table S1, Supporting Information). 19 Using coating conditions typical of slot-die coated films on a substrate near 100 °C, i.e., a wet film thickness of H = 5  $\mu$ m,  $au_{\rm evap} \approx 1$  s, and a diffusion coefficient of  $(D = 10^{-9} \text{ m}^2/\text{s})$  gives Bi = 0.025, which we assume to be sufficiently small to ignore vertical diffusion effects.<sup>20</sup> Overall, the model and results presented here are restricted to wide thin films far from any three-phase contact lines with  $Bi \ll 1$ , such that Marangoni and Rayleigh-Bernard instabilities can be ignored and vertical diffusion is unimportant.

**Transport Equations in the Confined Fluid.** The solute concentration as a function of space (x) and time (t) is determined by the solute species volume balance. Additionally, a total volume balance (solute and solvent) is also used to solve for the height of the film. The equations are then recast in terms of the solute volume fraction,  $\phi_{\Delta}$ . Details of the derivation are provided in the Supporting

Information (Section S.1). Changes in solute volume fraction and height of the liquid film in one dimension are given by

$$\frac{\partial \phi_{A}}{\partial t} = D \frac{\partial^{2} \phi_{A}}{\partial x^{2}} + \frac{D}{h} \frac{\partial h}{\partial x} \frac{\partial \phi_{A}}{\partial x} + \frac{E_{S,V}}{h} \phi_{A}$$
 (1)

$$\frac{\partial h}{\partial t} = -E_{S,V}(\phi_{A}) = -\beta \left( \frac{p_{\text{vap}} \overline{V}_{S}}{RT} \right) \left( \frac{(1 - \phi_{A})}{1 + \phi_{A} \left( \frac{\overline{V}_{S}}{\overline{V}_{A}} - 1 \right)} \right)$$
(2)

where D is the binary diffusion coefficient,  $E_{\rm S,V}$  is the evaporative volume flux with units of [m³/(s m²)], h is the wet film thickness,  $p_{\rm vap}$ is the solvent vapor pressure, R is the gas constant, and T is the temperature of the vapor phase. If partial molar volumes are constant, there is also only one binary diffusion coefficient, i.e.,  $D_A = D_S^{19}$  It is assumed that the liquid and vapor phases are isothermal and remain at the same temperature throughout the entire system for the duration of solidification and drying, i.e., the heat of solidification and evaporative cooling are not considered. Note that the second term on the right-hand side of eq 1 arises due to the nonuniform evaporation of solvent at the wet film height, h. The evaporative flux is defined following the work of Ternes et al. and is proportional to the mass transfer coefficient  $(\beta)$  and an evaporative driving force.<sup>20</sup> Raoult's law is used as the first approximation of the solution vapor pressure. Note that the right-hand side denominator  $[1 + \phi_A (\bar{V}_S/\bar{V}_A - 1)]$ comes from converting Raoult's Law expressed in mole fraction of solvent to volume fraction of solute. In the dilute limit of  $\phi_A \to 0$  or the single species limit of  $\overline{V}_{\rm S}/\overline{V}_{\rm A} \to$  1, eq 2 takes the familiar form of  $E_{\rm S,V} = \kappa (1-\phi_{\rm A})$  where  $\kappa$  is a mass transfer coefficient. In the concentrated limit of  $\phi_{\rm A} \to 1$ , then eq 2 takes the form of  $E_{\rm S,V} = \kappa'(1$  $-\phi_{\rm A}$ ) where  $\kappa'$  is a mass transfer coefficient modified by the species' molar volume ratio, i.e.,  $\kappa \overline{V}_A/\overline{V}_S$ .  $\beta$  is a function of the rate of air flow in the vapor phase and is assumed to be constant. The exact value of  $\beta$ will depend on the specific experimental drying conditions and solvent species; however, the magnitude is limited to a range of 2 orders in magnitude, i.e., natural convection to highly forced convection. <sup>21,22</sup>

It is useful to recast the time derivatives into a moving mesh for convenience of the numerical solution, such that the mesh node, n, can follow an arbitrary motion, in this case, the solidifying boundary. The following "moving mesh" formulation is defined

$$\zeta_i = \frac{i-1}{N-1} \qquad 1 < i < N \tag{3}$$

$$x_i = [b - x_{\text{xtal}}(t)]\zeta_i + x_{\text{xtal}}(t)$$
(4)

$$v_{ix} = \frac{\mathrm{d}x_i}{\mathrm{d}t} = (1 - \zeta_i) \frac{\mathrm{d}x_{\mathrm{xtal}}}{\mathrm{d}t} \tag{5}$$

where  $\zeta_i$  defines the fractional position of node i such that  $\zeta_1 = 0 \le \zeta_i$   $\le \zeta_N = 1$ , N is the total number of nodes in the domain, i is the node number,  $x_i$  is the position of the node along the domain, and  $v_{ix}$  is the velocity of the node i in the x-direction. The choice is made in eqs 3 and 4 that the nodes are always spaced uniformly. Thus, the final equations to be solved are given by

$$\frac{\mathrm{d}\phi_{\mathrm{A}}}{\mathrm{d}t} - \nu_{nx} \frac{\partial\phi_{\mathrm{A}}}{\partial x} = D \frac{\partial^{2}\phi_{\mathrm{A}}}{\partial x^{2}} + \frac{D}{h} \frac{\partial h}{\partial x} \frac{\partial\phi_{\mathrm{A}}}{\partial x} + \frac{E_{\mathrm{S,V}}}{h} \phi_{\mathrm{A}} \tag{6}$$

$$\frac{\mathrm{d}h}{\mathrm{d}t} - v_{nx} \frac{\partial h}{\partial x} = -E_{\mathrm{S,V}}(\phi_{\mathrm{A}}) \tag{7}$$

where d/dt is a time derivative following the motion of the nodes as opposed to the partial derivatives in eqs 1 and 2.

**Scaling.** The following natural scaling parameters have been chosen:  $\hat{x} = x/b$ ,  $\hat{h} = h/h_0$ , and  $\hat{t} = t/\tau_{\mathrm{D,x}}$  where  $\tau_{\mathrm{D,x}} = b^2/D$ , i.e., the characteristic lateral diffusion time scale. Substitution into eqs 6 and 7 gives

$$\frac{\partial \phi_{\mathbf{A}}}{\partial \hat{t}} - Pe\hat{v}\frac{\partial \phi_{\mathbf{A}}}{\partial \hat{x}} = \frac{\partial^2 \phi_{\mathbf{A}}}{\partial \hat{x}^2} + \frac{1}{\hat{h}}\frac{\partial \hat{h}}{\partial \hat{x}}\frac{\partial \phi_{\mathbf{A}}}{\partial \hat{x}} + Bi^* \left(\frac{1 - \phi_{\mathbf{A}}}{1 + \phi_{\mathbf{A}}\left(\frac{\overline{V}_{\mathbf{S}}}{\overline{V}_{\mathbf{A}}} - 1\right)}\right) \frac{\phi_{\mathbf{A}}}{\hat{h}} \tag{8}$$

$$\frac{\partial \hat{h}}{\partial \hat{t}} - Pe\hat{v}\frac{\partial \hat{h}}{\partial \hat{x}} = -Bi^* \frac{(1 - \phi_{A})}{1 + \phi_{A} \left(\frac{V_{S}}{V_{A}} - 1\right)}$$
(9)

All relevant coefficients relating to solvent properties and evaporative physics were combined into a dimensionless modified mass transfer Bi ( $Bi^*$ ), where  $Bi^* = Bi\Lambda^2 = (\beta h_0 \alpha_S/D)(b^2/h_0^2)$ .  $Bi^*$  is proportional to the ratio of the evaporation time scale normal to the air-liquid interface  $(\tau_{\text{evap}} = h_0/\beta)$  with the time scale of solute diffusion toward the solidifying surface parallel to the substrate ( $\tau_{D,x}$  =  $b^2/D$ ). Bi is the traditional mass transfer Biot number, defined as the ratio of the vertical solute diffusion time scale  $(\tau_{D,y} = h_0^2/D)$  to the evaporation time scale at the surface.  $\alpha_s$  is defined as the solvent vapor-liquid phase expansion coefficient, which is a ratio of the solvent liquid molar volume to the solvent vapor molar volume  $(\overline{V}_{\rm S}p_{\rm vap}/RT)$ . In this work, we include  $\alpha_{\rm s}$  within  $Bi^*$  for convenience.  $\Lambda$  is an aspect ratio defined by the half-distance between adjacent nuclei over the initial wet film height. When taken as a ratio of horizontal to vertical diffusion time scales over the initial bulk fluid,  $\Lambda^2 = \tau_{\rm D,x}/\tau_{\rm D,y} = b^2/h_0^2$ .  $\Lambda^2$  arises naturally from the non-dimensionalization of the transport equations and modifies the traditional Bi. Note that in addition to the assumption above, i.e., Bi  $\ll$  1, this model assumes  $\Lambda$  must be large enough that the time scale for horizontal diffusion between nuclei is significantly larger than the vertical time scale for diffusion through the wet film thickness, and vertical concentration gradients are negligible.  $\hat{\nu}$  is the dimensionless velocity of the solidifying boundary, defined as  $\hat{v} = v_{\text{xtal}}/v_0$  where  $v_0$  is a characteristic velocity. Nondimensionalizing the convective term introduces a dimensionless Pe, defined as Pe =  $v_0b/D$ . The characteristic velocity of the system may be selected depending on the desired numerical scaling or the choice of solidification growth model. In this work, the instantaneous initial velocity of the solidifying interface is used unless stated otherwise, i.e.,  $v_0 = v(x_{\text{xtal}}, t = 0)$ . The Pe is the ratio of the solidifying velocity time scale  $(\tau_v = b/v_0)$  between adjacent nuclei to the horizontal diffusion time scale  $(\tau_{D,x})$ , which are both defined parallel to the substrate.

To summarize

$$Bi^* = \left(\frac{\tau_{D,y}}{\tau_{evap}}\right) \left(\frac{\tau_{D,x}}{\tau_{D,y}}\right) = Bi\Lambda^2 = \left(\frac{\beta h_0}{D}\alpha_s\right) \left(\frac{b}{h_0}\right)^2$$

$$= \frac{\text{Evaporation velocity}}{\text{Horizontal diffusion velocity}}$$

$$Pe = \frac{\tau_{D,x}}{\tau_v} = \frac{\nu_0 b}{D} = \frac{k_g b}{D} (\phi_A^0 - \phi_A^{\text{sat}})$$

$$= \frac{\text{Solid growth velocity}}{\text{Horizontal diffusion velocity}}$$

The two derived dimensionless groups,  $Bi^*$  and Pe, may be used to compare the relative magnitudes of drying and solidification processes in the thin film. While simple to define, the terms used to define  $Bi^*$  and Pe represent complex, coupled, and/or nonlinear constitutive relationships that depend directly and/or indirectly on process parameters such as temperature and drying air velocity but also on formulation-specific properties like nucleation and solidification rates.

**Boundary and Initial Conditions.** The following initial conditions are specified at  $\hat{t}=0$ 

IC:
$$\phi_{A}(\hat{x}, \hat{t} = 0) = \phi_{A}^{0}$$
 (10)

$$IC:\hat{h}(\hat{x},\,\hat{t}=0)=1$$
 (11)

where  $\phi_A^0$  is the initial volume fraction of solute in the liquid phase. For simplicity, eq 10 specifies that the initial solute volume fraction in the liquid phase is uniform at  $\phi_A^0$  over the entire substrate. Note that the model imposes a uniform film height at  $\hat{t}=0$ , which is typical of the condition observed in the bulk of a wide coated film far from the three-phase contact line. For example, this assumption would be consistent with continuous coating techniques such as roll-to-roll slot-die coating of perovskite films, where the film is processed in a continuous steady state. At the symmetry boundary far from the solidifying interface ( $\hat{x}=1$  is the halfway point between adjacent nuclei), the following symmetry boundary conditions are applied

$$BC: \frac{\partial \phi_{A}}{\partial \hat{x}} \bigg|_{\hat{x}=1} = 0 \tag{12}$$

$$\frac{\partial \hat{h}}{\partial \hat{x}}\bigg|_{\hat{x}=1} = 0 \tag{13}$$

At the solidifying interface, eq 14 is derived from a volume balance of the solute at the moving interface

$$BC: \frac{\partial \phi_{A}}{\partial \hat{x}} \bigg|_{\hat{x} = \hat{x}_{xtal}} = Pe\hat{v}_{xtal}(\phi_{A}^{solid} - \phi_{A}|_{x_{xtal}})$$
(14)

 $\hat{\nu}_{xtal}$  is the velocity of the solidifying boundary relative to the substrate and  $\phi_A^{\text{solid}}$  is the volume fraction of the solute in the solid. Here, it is assumed that  $\phi_A^{\text{solid}} = 1$  meaning that the volume occupied by a molecule of solute is the same when it is dissolved in a solvent as when it has solidified. The velocity of the solid interface can then be expressed as a function of the liquid solute volume fraction at the interface  $(\phi_{A,xtal})$  and the diffusion of solute to the interface from the bulk

A rate equation is used to determine the velocity of the solidifying interface. Assuming first-order kinetics, the velocity of the solidifying boundary in 1D is defined as follows

$$v_{\text{xtal}} = k_{\text{g}}(\phi_{\text{A}}(x_{\text{xtal}}, t) - \phi_{\text{A}}^{\text{sat}}) \tag{15}$$

$$v_0 = v(x_{\text{xtal}}, t = 0) = k_g(\phi_A^0 - \phi_A^{\text{sat}})$$
 (16)

$$\hat{v}_{\text{xtal}} = \frac{\phi_{A}(x_{\text{xtal}}, t) - \phi_{A}^{\text{sat}}}{\phi_{A}^{0} - \phi_{A}^{\text{sat}}}$$
(17)

$$\hat{\nu}_0 = 1 \tag{18}$$

 $k_{\rm g}$  is the first-order rate constant,  $\phi_{\rm A}$  ( $x_{\rm xtal}$ ) is the volume fraction of solute in the liquid phase at the solidifying boundary, and  $\phi_{\rm A}^{\rm sat}$  is the solute volume fraction saturation, which is typically solute/solvent and temperature-dependent. The right difference ( $\phi_{\rm A}(x_{\rm xtal})$ , t) —  $\phi_{\rm A}^{\rm sat}$ ) represents the degree of supersaturation. Both  $v_{\rm xtal}$  and  $k_{\rm g}$  have units of [m/s]. Furthermore, the simplification of the solidification kinetics into a simple rate equation enables useful interpretation of known macroscopic kinetics without detailed knowledge of specific pathways or growth mechanisms. <sup>23,24</sup> More complex growth models may be used in place of the first-order rate law, such as a power law or Michaelis—Menten kinetics. For simplicity, only a first-order rate law was considered here. However, it will be shown that the growth of finite solid domains is only weakly dependent on the solidification kinetics, which means that a first-order rate law may be sufficient to approximate most cases.

**Solution Method.** Numerical solutions were obtained using the variable-step continuous implicit solver ODE15s in MATLAB. <sup>25</sup> The left-hand sides (time derivatives) of eqs 8 and 9 were solved using the state-dependent mass matrix (moving mesh) method. <sup>26</sup> The right-hand sides (spatial derivatives) were formulated as a set of explicit differential algebraic equations (DAEs) and discretized via finite differences. Solution convergence was defined by a relative tolerance of  $\varepsilon_{\rm rel} = 10^{-10}$  and an absolute tolerance of  $\varepsilon_{\rm abs} = 10^{-9}$ . Over the 1D domain (0  $\leq \hat{x} \leq$  1), a mesh of 200 nodes provided a reasonable

balance between solution accuracy and computational efficiency over the range of simulated conditions and was used for all presented results unless stated otherwise. All models were terminated when 99.9% of the initial solute volume was transferred from the liquid film into the growing solid. Further details regarding the numerical solution are provided in the Supporting Information (Section S.2).

Semi-Infinite Growth Model. In contrast to the finite domain model presented above, an alternative semi-infinite growth model was formulated to highlight the differences of unconfined growth without competition over solute by neighboring nuclei. For the semi-infinite case, the numerical mesh was fixed to a moving reference frame such that the width of the domain remained constant and both the lefthand boundary and right-hand boundary were moving at the same velocity equal to the solidification velocity (see Supporting Information, Section S.4). In this semi-infinite solution, the symmetry boundary conditions (eqs 12 and 13) remained the same; thus, the domain width needed to be extended such that the solute gradients generated by the growing solid did not interact with the opposite boundary. It was determined that a dimensionless width of 10 was sufficient to approximate a semi-infinite bath (see Supporting Information, Section S.3). Note that the growth of a single solid domain in an infinite bath is the semi-infinite diffusion-convection problem, which has a known analytical solution in the absence of

**Model Validation.** Two limiting cases were used to verify the numerical accuracy of the model: (1) Pe = 0, which represents solvent drying without solidification and (2)  $Bi^* = 0$ , which represents solute solidification without drying.

Drying without Solidification, Pe = 0 Limit. In the absence of solidification (i.e., Pe = 0), only the wet film height changes due to evaporation, since no solid forms. Thus, eq 9 may be rewritten in terms of the wet film height by recognizing that the overall volume fraction of solute is inversely proportional to the uniform decrease in wet film height, i.e.,  $\phi_A = \phi_A^0 h_0 / \hat{h}$ 

$$\frac{d\hat{h}}{d\hat{t}} = -Bi^* \left( 1 + \frac{\phi_A^0 \hat{h}_0}{\hat{h} - \phi_A^0 \hat{h}_0} \frac{\overline{V}_S}{\overline{V}_A} \right)^{-1}$$
(19)

For convenience, we define  $\hat{h}_s = \phi_0^A \hat{h}_0 \overline{V}_S / \overline{V}_A$  as the uniform dry film thickness scaled by the ratio of solute and solvent molar volumes. Integrating and solving explicitly for  $\hat{h}$  gives

$$\hat{h}(\hat{t}) = \phi_{A}^{0} \hat{h}_{0} + \hat{h}_{s} W \left( \frac{\hat{h}_{0} - \phi_{A}^{0} \hat{h}_{0}}{\hat{h}_{s}} \exp \left[ -\frac{1}{\hat{h}_{s}} B i^{*} \hat{t} + \frac{\hat{h}_{0} - \phi_{A}^{0} \hat{h}_{0}}{\hat{h}_{s}} \right] \right)$$
(20)

where W is the Lambert W function or product logarithm. When  $\hat{t} \to \infty$ , the time-dependent argument of W goes to zero and W(0) = 0. The height of the wet film approaches the theoretical dry film thickness, i.e.,  $\hat{h}(\hat{t} \to \infty) = \phi_0^A h_0$ . This simplification allows for an analytical expression for film height and solute volume fraction, which is detailed in the Supporting Information (Section S.5).

Figure 2 shows the analytical solution for both the change in the average wet film height  $(\hat{h})$  and the change in solute volume fraction  $(\phi_A)$  over time with the corresponding numerical model results. The wet film height approaches  $\hat{h}=0.25$  as  $\hat{t}\to\infty$ , which is the average uniform dry film thickness predicted by the initial conditions  $\phi_A^{\ 0}=0.25$  and  $\hat{h}_0=1$ . The solute volume fraction approaches  $\phi_A=1$  as  $\hat{t}\to\infty$ , which represents the total aggregation of available solute in the domain. In this limit, all solutions are shown to collapse to a single curve when the time is scaled by the  $Bi^*$ .

Solidification without Drying,  $Bi^*=0$  Limit. In the limit of no drying, i.e.,  $Bi^*=0$ , eqs 8 and 9 reduce to the case of diffusion-driven solidification in the bulk. The model assumes that the solid height is always equal to the wet film height at the interface during solidification. In the limit of  $Bi^*=0$ , the constant wet film height results in a rectangular solid, i.e.,  $\hat{h}_{xtal}(\hat{x},\hat{t})=1$ , see Figure 3a. The rate at which the solid interface advances through the bulk is dependent on solidification kinetics (Pe) and diffusion.

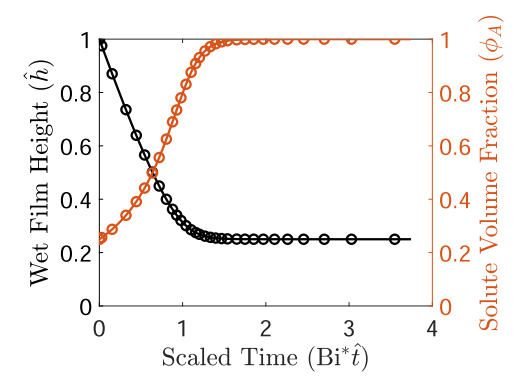


**Figure 2.** Wet film height over time for the numerical (circles) and analytical solution (solid line), which also match the solution derived by Ternes et al. for the case where only drying is considered.<sup>20,27</sup> The secondary axis (orange) displays concentration over time, which is uniform throughout the wet film during drying due to the uniform initial condition. Initial solute volume fraction is 0.25. Residuals comparing the numerical and analytical solution are presented in the Supporting Information (Section S.3).

Similar to the limit of Pe=0, an analytical expression for nondiffusion-limited growth was derived (eq 21, details provided in the Supporting Information, Section S.6). Here, a lumped parameter approach was taken that assumes fast diffusion in the liquid film, such that the solute volume fraction throughout the wet film is treated as an average value across the domain

$$\hat{x}_{xtal} = \frac{\phi_{A}^{0} - \phi_{A}^{sat}}{1 - \phi_{A}^{sat}} - \frac{1 - \phi_{A}^{0}}{1 - \phi_{A}^{sat}}$$

$$W\left(\frac{\phi_{A}^{0} - \phi_{A}^{sat}}{1 - \phi_{A}^{0}} \exp\left[-\frac{(1 - \phi_{A}^{sat})^{2}}{(1 - \phi_{A}^{0})(\phi_{A}^{0} - \phi_{A}^{sat})}Pe\hat{t}\right]$$

$$+ \frac{\phi_{A}^{0} - \phi_{A}^{sat}}{1 - \phi_{A}^{0}}$$
(21)

As  $\hat{t} \to \infty$ , the location of the solid–liquid interface grown without drying reaches the limit  $\hat{x}_{\text{xtal}}(\hat{t} \to \infty) = (\phi_{\text{A}}^0 - \phi_{\text{A}}^{\text{sat}})/(1 - \phi_{\text{A}}^{\text{sat}})$ . In this case, time may be scaled by Pe in order to produce a master curve for the case where diffusion is very fast and gradients do not develop in the bulk. As the solidification rate increases (increasing Pe), the scaled solutions begin to deviate as solute transport to the solidifying surface is limited by diffusion.

The well-known LaMer model for diffusion-driven growth provides an additional comparison with our numerical and analytical results. The LaMer model was originally formulated in a seminal work to describe particle growth from solution, and the 1D case is detailed in the Supporting Information (Section S.7) for completeness.  $^1$  Here,  $\phi_A^0$  = 0.25 and  $\phi_A^{\rm sat}$  = 0.1, which is within the range of supersaturation predicted by theory and experiments.  $^{28}$  As an approximation of growth into a semi-infinite bulk, the LaMer model predicts that growth approaches a limit defined by the degree of supersaturation ( $\phi_A^0 - \phi_A^{\rm sat}$ ). However, in a confined system, the bulk domain is finite and shrinks as the solid interface grows. Thus, the position of the interface actually approaches ( $\phi_A^0 - \phi_A^{\rm sat}$ )/(1 -  $\phi_A^{\rm sat}$ ) as  $\hat{t} \to \infty$ .

Figure 3c shows that, at short times, LaMer's model represents the upper limit for the initial growth rate. LaMer's model, though originating from Fick's law, actually neglects diffusion across the bulk by imposing boundary conditions corresponding to saturation at the growing particle interface and a flux equal to the growing particle rate at the far boundary. Therefore, the fast diffusion lumped parameter solution and LaMer's model only remain accurate at shorter initial times as diffusion increasingly limits solute transport to the interface (and solute concentration gradients through the bulk are negligible). In other words, the LaMer model only accurately predicts growth at early times when solute diffusion to the growing interface is faster than the depletion of solute near the interface by the growing solid.

These two limiting cases served as a model validation to ensure that the model was capable of capturing the important physics of drying and growth. In both cases, our model was able to accurately capture the expected result. We now look at the less intuitive results of mixed solid growth and drying.

### ■ RESULTS AND DISCUSSION

The results and discussion are organized as follows: first, a base case result is described so that the complex effects of solute diffusion, solidification rate, and decreasing wet film height on the solid profile can be examined in detail. By estimating substrate coverage based on the end point of the profile relative to the domain boundary, the predicted solid profiles give a first approximation of quality in a real coating. Specifically, in Figure 4c, the termination of this curve at a value  $\hat{x} < 1$  indicates the presence of a void from the point of termination up to the start of the next solid across the boundary. Finally, these results are combined to construct a generalized process map and case study that provides a quantitative guide to designing solution-based thin film coating processes

**Detailed Example Case.** Figure 4 displays a typical set of model results detailing the effects of coupled solidification and drying on the solute volume fraction, wet film height, deposited solid profile, and growth velocity. Both solidification and evaporation were chosen to be similar in magnitude (Pe = 1 and  $Bi^* = 1$ ) and the initial conditions correspond to a uniform film with  $\phi_A^{\ 0} = 0.25$  and  $\phi_A^{\ \text{sat}} = 0.1$ . At short times, Figure 4a shows that the solute concentration near the solid—

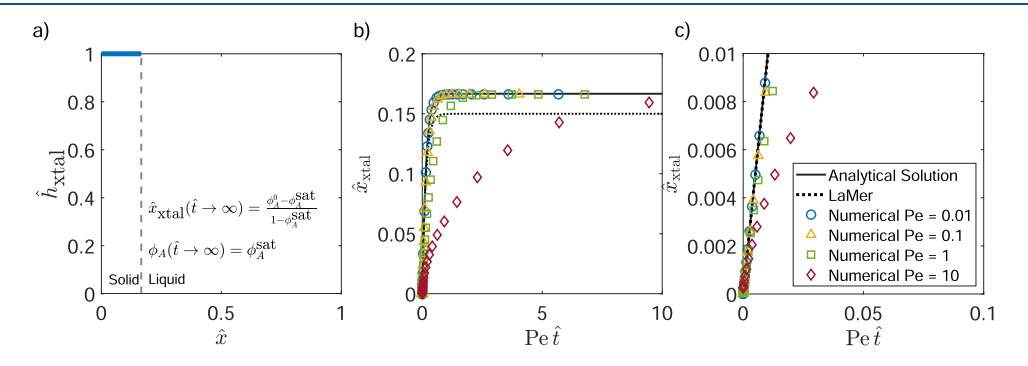


Figure 3. (a) Solid profile formed without drying  $[Bi\ (0) = 0]$ . Dashed line separates solid (left) and liquid bulk (right). (b,c) Comparison of solid interface position over time between the analytical solution (eq 21, solid line), the 1D Cartesian LaMer diffusion-driven growth model (dashed line), and numerical results as Pe is increased. Pe = 0.01 (circles), Pe = 0.1 (triangles), Pe = 1 (squares), and Pe = 10 (diamonds).

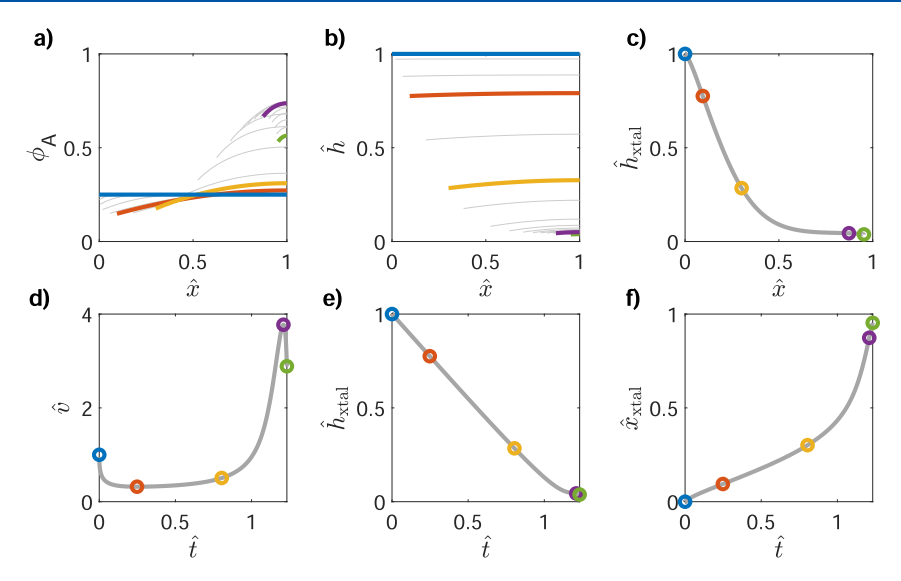
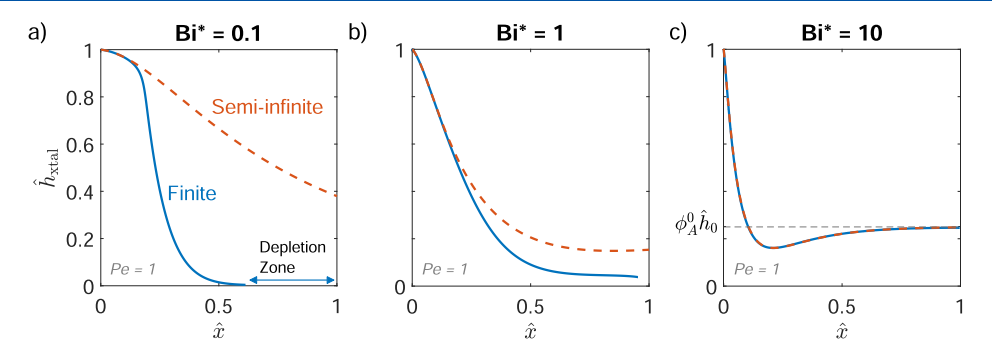


Figure 4. Example results from a semi-infinite quasi-2D drying and solidification model. (a) Solute volume fraction in the liquid as a function of position. (b) Dimensionless wet film height as a function of position. Successive curves denote separate numerical solutions over time for parts (a,b). (c) Solid interface height as a function of position, which estimates a deposited solid profile. (d) Velocity of the interface over time. (e) Height of the wet film at the solid interface over time. (f) Position of the solid interface over time. Thick lines and circled points correspond to the same time points:  $\hat{t} = 0$  (blue),  $\hat{t} = 0.248$  (orange),  $\hat{t} = 0.804$  (yellow),  $\hat{t} = 1.209$  (purple), and  $\hat{t} = 1.232$  (green). All results are for the case where Pe = 1,  $Bi^* = 1$ ,  $\phi_A^{\ 0} = 0.25$ , and  $\phi_A^{\ sat} = 0.1$ .



**Figure 5.** Comparison between predicted solid profiles for finite (solid blue) or a semi-infinite (orange dashed) model for a characteristic Pe = 1 for (a)  $Bi^* = 0.1$ , (b)  $Bi^* = 1$ , and (c)  $Bi^* = 10$ .

liquid interface rapidly approaches  $\phi_{\mathrm{A}}^{\mathrm{sat}}$ , while the concentration far from the interface remains near  $\phi_A^0$  (increasing slightly due to evaporation) initially. Recall that the constitutive growth rate chosen in eq 15 is linear so the concentration of the interface is reflected by the solid interface velocity in Figure 4d  $[\hat{\nu}_{xtal} \propto (\phi_{A,xtal} - \phi_A^{sat})]$ . At  $\hat{t} = 0.248$ (orange curve), the velocity of the interface reaches a minimum as the growing solid depletes solute at a rate that is balanced by the replenishment of solute via diffusion and evaporation. The constant growth rate is reflected by the linear increase in the interface position over time in Figure 4f. As  $\hat{t}$  = 0.804 (green curve), the wet film height decreases so that evaporation begins to appreciably concentrate the solute and accelerate the growth of the solid. In this regime,  $d\hat{h}/d\hat{t}$  is constant (Figure 4e); however, the relative effect of evaporation on solute concentration increases (compared to diffusion and growth) as the wet film height decreases (the evaporation term in eq 8 is proportional to  $\phi_A/h$ ).

At  $\hat{t} = 1.209$  (purple), evaporation drives the growth rate to a maximum velocity and the majority of the predicted solid profile has been established (Figure 4c). The velocity reaches a maximum nearly four times greater than the initial growth rate. For the conditions presented in this work, up to a 6-fold

difference in growth rate from the initial growth velocity is achievable. This may be shown from a simple calculation based on the known solute solubility and reaction rate laws, i.e.,  $\hat{\nu}_{\rm max}/\hat{\nu}_0=(\phi_{\rm A}^{\rm stal}-\phi_{\rm A}^{\rm sat})/(\phi_{\rm A}^0-\phi_{\rm A}^{\rm sat})$ . Here,  $\phi_{\rm A}^{\rm \ stal}=1$ ,  $\phi_{\rm A}^{\rm \ sat}=0.1$ , and  $\phi_{\rm A}^{\ \ 0}=0.25$ , thus  $\hat{\nu}_{\rm max}/\hat{\nu}_0=6$ . Such a significant variation in growth rate could affect the chemical and physical attributes of a real solid, including composition partitioning, defects, and grain size distribution.

Importantly, the substrate coverage and connectivity of neighboring solids are approximated by the final position and height of the solid (Figure 4c, green). The predicted solid profile in Figure 4c is a parametric plot of the height (Figure 4e) and position (Figure 4f) of the interface over time and represents a cross-section of the solid's topography over the substrate ( $\hat{h} = 0$ ). The conclusions presented in this study largely rely on constructing similar solid profiles to predict the average degree of substrate coverage based on the end point of the solid profile relative to the  $\hat{x} = 1$  symmetry boundary. It is worth noting that a corresponding axisymmetric model, corresponding to eqs 8 and 9 can be derived and solved (not shown here) to better approximate a spherulite-like domain. However, the symmetry plane at x = b no longer become physically relevant in the axisymmetric case. In reality,

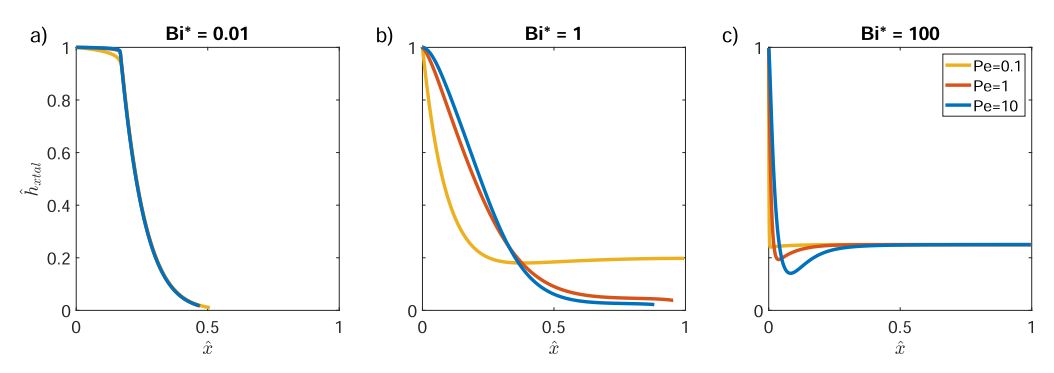


Figure 6. Domain thickness profiles comparing the effect of changing Pe at  $Bi^*$  for the (a)  $Bi^* = 0.01$  disconnected coating regime, (b)  $Bi^* = 1$  transition regime, and (c)  $Bi^* = 100$  uniform coating regimes.

there would be other nuclei located at discrete angles,  $\theta$ . Nonetheless, the results were computed considering the 1D axisymmetric versions of the model equations and boundary conditions to determine if the trends in Figure 4 are general for different geometries. Interestingly, the results of the axisymmetric model (Supporting Information, Section S.8) show the same trends as the Cartesian model and only differ slightly in the solid profiles. Thus, we expect that these results are translatable to more realistic solid growth scenarios that involve radial growth. The remainder of the paper uses these process—structure relationships to examine how substrate coverage and differences in solid thickness profiles emerge from differences in the drying and solidification behavior of thin films.

Confined Growth Limits Coverage at Low Bi\*. Confined growth occurs when two adjacent growing solids deplete interstitial solute over a length scale greater than half their separation distance, such that the growth rates of two neighboring solids are a function of their proximity. To illustrate this point, a direct comparison between the previously described finite model and the semi-infinite model was made. The semi-infinite growing solid has access to an unlimited quantity of solute in the bulk transported through the boundary at  $\hat{x} = 1$ , while the finite solid is limited by the initial solute present in the domain. Figure 5a shows that at low Bi\*, the solid profile of the finite model significantly diverges from the semi-infinite solution, illustrating the necessity of including interdomain competition in order for the model to manifest the phenomenon of depletion and void formation. When Bi\* is small, the length scale for horizontal diffusion exceeds the midpoint between adjacent growing solids and the growth is confined. Note that at early times, the semi-infinite and finite profiles overlap as evaporation is the same in both cases and the initial growth depletes the local solute from supersaturation to saturation. At  $Bi^* \ll 1$ ,  $\tau_{\rm D,x} \ll \tau_{\rm evap}$  such that evaporation does not appreciably concentrate the solute in the bulk and gradients across the domain are minimized. The finite and semi-infinite profiles diverge around  $\hat{x} \approx 0.2$  in Figure 5a. For the finite model, solid growth depletes solute and the solute concentration in the liquid film between adjacent domains decreases to near saturation. Thus, the solid in the finite growth model can continue to grow only when evaporation increases the solute concentration above saturation. In contrast, the semi-infinite model allows the solid to grow continuously since the solute is replenished via diffusion far from the solid-liquid interface.

A depletion zone is defined by the presence of the bare substrate after complete evaporation, as shown in Figure 5a.

This occurs due to the confined volume between solid domains, which limits the number of molecules available for growth. At  $Bi^*=0.1$ , the confined solid terminates (99.9% solute consumed) at approximately  $\hat{x}=0.6$ , leaving nearly 40% of the substrate uncoated. The initial growth of the finite solid produces a tall, "plateau-like" shape since solid growth is faster than the decrease in the height of the liquid interface, depleting the bulk of the solute and leading to a sharp drop-off in solid height. Depletion zones are defined by the length of the uncoated substrate and are found to be significant when  $Bi^* \ll 1$ . Confined solid growth leading to depletion zones is expected to form highly disconnected coatings with poor substrate coverage.

At  $Bi^* = 10$  (Figure 5c), the finite growth model shows no effects of confinement, which is denoted by the overlap between semi-infinite and finite model solutions. At all times during growth, the depletion depth from the growing solid front is very small since the solute in the bulk is sufficiently concentrated through solvent evaporation and  $au_{\rm evap} \ll au_{\rm D,x}.$ Therefore, at sufficiently high Bi\*, the spacing between neighboring solid domains does not play a role in the shape and thickness profile, and the thickness of the solid domain approaches the theoretical average thickness  $(h_{\text{avg}} = h_0 \phi_{\text{A},0})$ near the symmetry boundary ( $\hat{x} = 1$ ). Under these conditions, the solute concentration far from the solid interface approaches  $\phi_{\rm A} \approx 1$  due to high evaporation rates and the system is "meltlike" as the degree of supersaturation exceeds what may be considered reasonable for most salt-based solute-solvent systems and is more similar to highly concentrated polymers or solidifying melts.

As  $Bi^*$  increases, the "disconnected" solid profile becomes increasingly "connected" to its adjacent neighbor at the symmetry plane and the uncoated depletion zone diminishes. This transition occurs within a narrow range of intermediate  $Bi^*$  values  $(0.1 < Bi^* < 10)$ . Within the transition regime, the solid profile shape is sensitive to both  $Bi^*$  and Pe. Solid profiles produced at either high or low  $Bi^*$  ( $Bi^* \ge 10$  and  $Bi^* \le 0.1$ ) are relatively insensitive to order of magnitude changes in Pe. This is further described in Figure 6.

At low  $Bi^*$ , the growth of the solid domain is driven by the initial supersaturation and solidification kinetics. For  $Bi^* = 0.1$ , an inflection point occurs at the knee of the curve corresponding to a transition into a drying-driven growth regime, at approximately  $\hat{x} = 0.18$  and  $\hat{h} = 0.9$ . As  $Bi^*$  increases, the inflection point appears earlier in the thickness profile corresponding to an overall shift toward drying-dominated growth. This shift corresponds to the minimum in growth velocity over time, where the initial solidification rate is fast

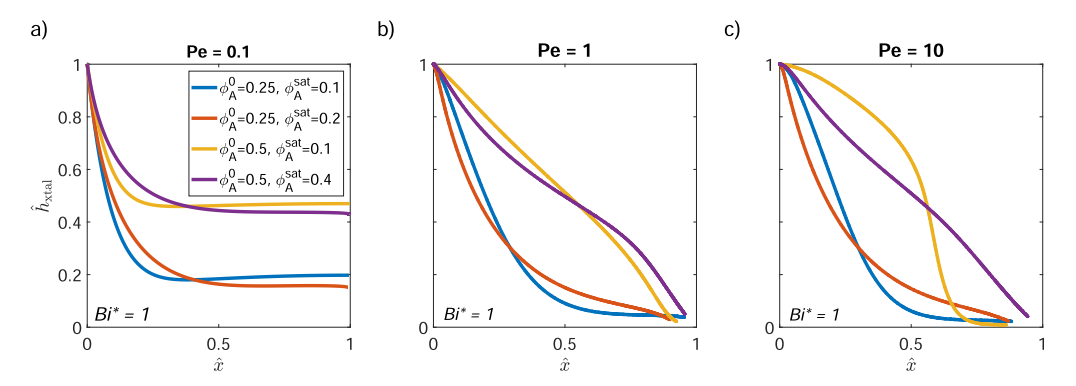


Figure 7. Solid height profiles for different Pe at  $Bi^*=1$ . Panels (a) Pe=0.1, (b) Pe=1, and (c) Pe=10 contain curves with different degrees of supersaturation corresponding to  $\phi_A^{\ 0}=0.25$  and  $\phi_A^{\ sat}=0.1$  (blue),  $\phi_A^{\ 0}=0.25$  and  $\phi_A^{\ sat}=0.1$  (orange),  $\phi_A^{\ 0}=0.5$  and  $\phi_A^{\ sat}=0.1$  (yellow), and  $\phi_A^{\ 0}=0.5$  and  $\phi_A^{\ sat}=0.4$  (purple).

until the local solute at the interface is depleted and the velocity does not increase again until evaporation drives the concentration of solute in the bulk. For  $Bi^* = 10$ , nearly the entire solid profile is controlled by evaporation. Under these conditions, the growth velocity is always increasing due to evaporation, increasing supersaturation at a rate that exceeds the consumption of solute at the solidifying boundary. As Bi\* becomes large (e.g., at  $Bi^* = 10$ ), a local minimum in the solid profile emerges around  $\hat{x} \approx 0.2$  due to extremely rapid local drying at the solidification interface. The height of the wet film is reduced more rapidly near the solidifying interface due to the greater solvent concentration compared to the bulk wet film far from the solidifying boundary. At high Bi\*, the assumption that the height of the growing domain is always equal to the height of the wet film at the interface produces an initial "spike" at  $\hat{x} = 0$  to  $\hat{h} = 1$ . Since this is the simplest approximation possible with a quasi-2D model, it is likely that this artifact would not be present with a 2D growth model nucleated in the bulk or at the substrate surface, which may in fact produce dimpled domains at high Bi\*. In a real system, solution is likely also present above the growing solid, at both early times when the size of a nuclei is less than the height of the wet film  $x_{\text{xtal}} < h_0$ , and during growth since the saturation volume fractions are often less than 0.25. While a 2D model would certainly improve the quantitative solid profile predictions, the overall coverage of the solid is not expected to be significantly different between the 2D model and the results presented here. The reason for this is that the vertical growth of the solid is limited to an early time since depletion of the solute above the solid would happen relatively quickly. Thus, most of the solid coverage is determined by the horizontal growth of the solid domain.

Uniform solid films are produced at high  $Bi^*$ , which can be achieved through engineering of the drying rate  $(\beta)$ , nucleation rate and time (b), solvent properties  $(\alpha_S, p_{vap})$ , or coating parameters  $(h_0)$ . However, the relationship of these parameters is not always intuitive. For example, one might posit that an increasing nucleation rate might lead to more uniform films. However, a higher nucleation rate will lead to more closely spaced nuclei and smaller b, which would decrease  $Bi^*$  and lead to a worse quality film. This occurs because closely spaced nuclei increase the effect of confinement  $(Bi^* \propto b^2)$ , leading to more incomplete coverage through competition over solute between adjacent solid domains. In real systems, it is likely that the strong coupling between common variables (such as temperature and drying air velocity) that are used to increase

the nucleation rate also simultaneously lead to faster evaporation rates (higher  $Bi^*$ ) that may improve film quality. This interplay between nucleation rate and evaporation rate is most important when  $Bi^* \approx 1$ , i.e., the transition regime, which is sensitive to changes in Pe or  $Bi^*$ . These results signify the importance in developing nucleation models that take into account process parameters such as temperature and concentration.

Pe Only Affects Morphology in the Transition **Regime.** The previous section showed that Bi\* significantly affects the solid profile and determines whether adjacent domains are connected or disconnected. Figure 6 shows that for the finite model, solidification kinetics characterized by Pe have only a small impact on solid thickness profiles. At very fast or slow evaporation rates ( $Bi^* \ge 100$  and  $Bi^* \le 0.01$ ), orders of magnitude changes in Pe have nearly negligible effects on the predicted solid profile, and important features such as the depletion zone width and thickness approaching the symmetry plane remain unchanged. Only within the transition regime (Figure 6b,  $0.1 \le Bi^* \le 10$ ) are changes in Pe found to significantly impact the solid profile and connectivity. In this work, the range of Pe,  $0.1 \le Pe \le 10$ , was chosen for its relevance to crystallizing salt systems, which tend to have fast (mm/s) linear growth rates. 29,30 We observe from Figure 6 that for low and high values of Bi\*, there is little to no effect of Pe on the overall shape of the solid. However, when  $Bi^* = 1$ , see Figure 6b, the effect of Pe is very pronounced. For Pe = 1and 10, the solids show thin connected regions across the entire domain. However, for Pe = 0.1 (slow kinetics compared to diffusion), the shape of the solid profile is very similar to Figure 6c with a uniform film (thickness  $h_{xtal} = \phi_A^0 \hat{h}_0$ ) connecting adjacent domains. This result suggests that for  $Bi^* \approx 1$ , increasing the solidification time scale relative to the diffusion time scale is a method of improving solid coverage.

The fact that Pe plays a major role in the solid connectivity and morphology at moderate modified Bi, i.e.,  $Bi^*=1$ , means that we must also consider the contributions of convection. Recall that in the models presented here, we assume that the only mechanism of solute transport is diffusion. However, it is easy to think of scenarios where the dominant transport mechanism is rotational convection cells, such as those induced by Rayleigh–Bernard or Marangoni effects. Such convective flows could significantly enhance the transport of solute to the interface, which would largely decrease the effective Pe and  $Bi^*$ .  $^{18,31,32}$  Therefore, it is not clear to what degree Pe may be controlled in practice. For example, by

heating the substrate from below (Rayleigh–Bernard) and/or from above (Marangoni), it is possible that significant convection within the thin films occurs, which would increase the diffusion velocity and thus decrease Pe. In practice, it is reasonable that thin film dynamics are limited to very low Pe. In any case, the conclusions and trends are the same for convection, and one need only consider the contribution of convection to the magnitude of Pe.

**Solubility and Supersaturation.** Figure 7 shows that overall,  $\phi_A^{\ 0}$  and  $\phi_A^{\ sat}$  have a minimal effect on the solid profile shape and connectivity, even within the transition regime at moderate  $Bi^*$ . The solute concentration and solubility  $(\phi_A^{\ sat})$  are often the first experimental parameters to be optimized for poor thin film coatings. Solubility can be directly tuned via temperature. Here,  $\phi_A^{\ 0}$  is used to control the total volume of the solute present within the initial wet film, but it is also the solute concentration at nucleation  $(\phi_A^{\ 0})$ , which is difficult to predict experimentally. In practice, the average thickness  $(\hat{h}_{avg} = \phi_A^0 \hat{h}_0)$  is usually a critical quality attribute so the range of allowable concentrations may be limited by the achievable coating thicknesses for any given coating process.

Figure 7a,b shows that at low to moderate Pe, 0.1 < Pe < 1, a greater  $\phi_{\rm A}^{\ 0}$  generally only leads to a greater average thickness. The shapes of the solid profiles are only slightly affected by  $\phi_{\rm A}^{\rm sat}$  due to changes in the rate constant  $k_{\rm g}$  needed to maintain the same Pe for each set of results (assuming the b and D are constant). At high Pe = 10 (Figure 7c), increasing  $\phi_A^{0}$ increases confinement, resulting in the same "plateau-like" growth observed at low  $Bi^* = 0.01$  (Figure 6) for  $\phi_A^0 = 0.25$ and  $\phi_A^{\text{sat}} = 0.1$ . The plateau becomes less apparent as  $\phi_A^{\text{sat}}$  increases ( $\phi_A^{\ 0} = 0.5$ ,  $\phi_A^{\text{sat}} = 0.4$ , purple curve). A higher degree of supersaturation has a greater  $v_0$ , which for the same Pe results in a larger length-scale for diffusion transport of the solute. This effectively increases the ratio of the diffusion length-scale to the half-distance between solid domains. As explained earlier, once this ratio approaches and exceeds unity (at  $Bi^* = 1$ ), the gap between domains is depleted and the solids are disconnected.

Outside of the transition regime, when  $Bi^* \ge 100$  and  $Bi^* \le 0.01$ , changing  $\phi_A^{\ 0}$  or  $\phi_A^{\ sat}$  has no significant effect on the diffusion length-scale and thus the solid profile. The only appreciable change is an increase or decrease in the average solid thickness (see Supporting Information, Section S.9).

Coating Quality Process Map. As discussed in prior sections and shown in Figures 5 and 6, Bi\* largely controls the connectivity and uniformity of the deposited solid in an evaporating thin film. Therefore, it is interesting to consider the effect of experimental parameters on the solid coverage of the final films. Bi\* is composed of two independent dimensionless groups, the traditional Bi and the square of the aspect ratio,  $\Lambda^2$ , which together determine the experimentally achievable substrate coverage. Bi accounts for the coating and drying process parameters, such as the evaporation mass transfer coefficient, solvent vapor pressure, and coating thickness. The magnitude of Bi is predominately determined by the choice of solvent, i.e., vapor pressure and binary diffusion coefficient.  $\Lambda$  is a function of the nucleation flux, solute solubility (saturation concentration), and film thickness and must be determined experimentally.

Figure 8a represents a process map of Bi and  $\Lambda^2$ , where the characteristic growth rate to diffusion ratio is uniform for all of the conditions represented in the map (i.e., Pe = 1). The diagonal lines represent the final film solid coverage calculated

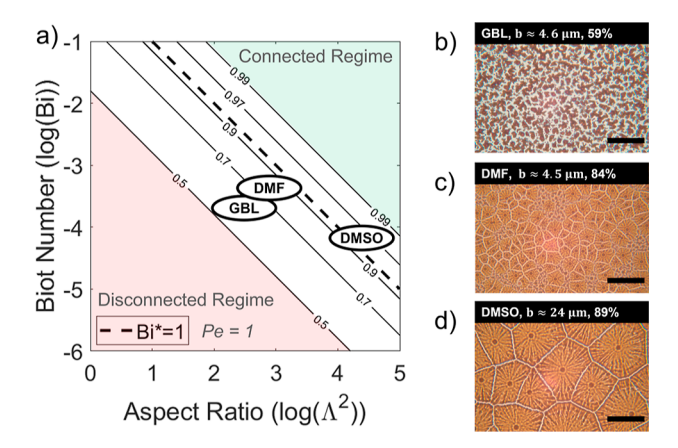


Figure 8. (a) Coating quality process map of Bi vs  $\Lambda^2$  with lines corresponding to fractional substrate coverage at 99.9% total solute volume solidified for Pe=1. Labels for GBL, DMF, and DMSO approximate the position of common pure solvents used in the processing of the MAPbI<sub>3</sub> thin films shown. Films were made via slot-die coating at 100 °C for 0.5 M MAPbI<sub>3</sub> in (b) GBL, (c) DMF, and (d) DMSO with measured b nuclei half-spacing and actual coverage measured via ImageJ (see Supporting Information, Section S.11). Scale bars are 40  $\mu$ m.

by the quasi-2D model. The dashed line corresponds to  $Bi^* = 1$ . There are two distinct regions corresponding to poorly connected solid domains (substrate coverage <0.5) and well connected solid domains (substrate coverage >0.99). Note that Pe does not depend on  $\Lambda$ , and smaller values of Pe would shift the coverage lines toward smaller values of  $\Lambda$ , making it easier to reach higher coverages, as described in detail in Figure 6. A moderate value of Pe = 1 is observed to be in good agreement with the experimental results. Note that the process map does depend on the value of Pe and would need to be redrawn for specific cases.

Several thin film coating and drying experiments were carried out to test the validity of the process map. The archetypal perovskite photovoltaic salts methylammonium iodide (MAI) and lead iodide (PbI<sub>2</sub>) were dissolved at a 1:1 stoichiometric ratio to make 0.5 M solutions of methylammonium lead iodide (MAPbI<sub>3</sub>) in the solvents gamma butyrolactone (GBL), dimethylformamide (DMF), and dimethyl sulfoxide (DMSO). The three solvents were chosen for their very different magnitudes of Bi, with DMF being the highest due to having a vapor pressure nearly four times greater than DMSO and nearly seven times greater than GBL at 100 °C. Additional values of *Bi* calculated for common perovskite processing solvents are given in Table S1; see Supporting Information. Wet films were coated targeting 5  $\mu$ m, with a stage temperature of 100 °C onto glass substrates. A was measured using microscopy images, as seen in representative images in Figure 8b-d. The value of b, ergo  $\Lambda$ , is significantly different for the solvent choices. To calculate  $\Lambda$ , the spacing between crystalline domains was determined from the topdown bright-field microscope images in Figure 8b-d, and the height h was estimated based on cross-sectional SEM (see Supporting Information, Section S.11). In doing so, we assume that the domain boundaries evident in the dry film remain unchanged by annealing; that is, no significant domain consolidation or ripening occurred in the solid state; this assumption was not tested further. Solid coverage area for each film was determined using ImageJ image processing software. Detailed calculations for each thin film sample shown in Figure

8b-d are provided in the Supporting Information (Section S.11).

Placing the experimental conditions for each solvent system onto the process map in Figure 8a shows an acceptable agreement between the predicted coverage and the actual films. The actual coverage for GBL (59%) and DMF (84%) was surprisingly close to the predicted values of roughly 60% and 80%, respectively. As seen in Figure S12, the coverage area via the image processing procedure falsely counts areas near the center of the crystal domain as not covered. Thus, the calculated coverage for DMSO (89%) is slightly lower than expected. However, the coverage area calculation could be improved by better thresholding algorithms, which are outside the scope of this work.<sup>33</sup> Overall, these experiments show excellent agreement with the quasi-2D model presented here.

Although the model does seem to correlate to experimental results, the image analysis has also highlighted some important limitations of the model. For example, the model assumes a single nucleation event; however, the images clearly show a large number of smaller secondary crystals (or nuclei) between the larger primary domains (most clearly visible for the GBL film). It is evident from in situ microscopy (not shown) that these secondary domains nucleate after the larger primary domains have formed. In its current form, the model allows for the solute volume fraction to rise significantly above the initial degree of supersaturation, approaching 1 in some cases. It is likely that as the solute volume increases toward 1, there may be either a secondary nucleation event in the liquid phase or the liquid phase undergoes an "amorphous" solidification, which could crystallize later. One could imagine a secondary nucleation event incorporated into the model at the symmetry plane when the solute volume fraction reaches a threshold supersaturation for a sufficient length of time. It is likely that this case would be relevant only at moderate to high Bi\*, where solute volume fractions approach 1. However, at high Bi\*, the evaporation is already sufficiently large to produce uniform films, such that the introduction of additional nuclei would not alter the overall trends in shape and coverage. At moderate Bi\*, the inclusion of additional nuclei would only serve to reduce the local aspect ratio,  $\Lambda$ , increasing competition for solute and leading to a premature termination of the primary crystal growth and thus poorer film coverage. While secondary nucleation events have been directly observed experimentally, subsequent nucleation events are outside the scope of this preliminary model, and the overall trends observed are not expected to differ.

Other important considerations include the effect of solvent-solute coordination and antisolvents during processing. All three solvents used in this study have been shown to coordinate with lead iodide with affinity increasing with their donor numbers, i.e., increasing in order of GBL, DMF, and DMSO.34,35 Our model results may explain why solvent mixtures have been employed with considerable success. For example, DMF-DMSO mixtures have shown very high coverage in the formation of perovskite films. 11,36 The mixture of these two solvents could act favorably in tuning Bi and  $\Lambda$ separately, e.g., DMF allows for a high Bi and DMSO allows for a large  $\Lambda$  by forming a strong solvent-solute complex.<sup>3</sup> Antisolvents are commonly employed in spin coating to produce void-free films. Even though our model was derived based on simple coating and drying physics, the results presented here can be put into the context of the antisolvent method. More specifically, the antisolvent drives the solute to

precipitate by significantly decreasing the solubility of the solute in the solvent mixture. The rate of solvent mixing is orders of magnitude greater than the solvent removal rates achievable by evaporation. In other words, the success of the antisolvent method is equivalent to the predictions for a high  $Bi^*$ . Future work is underway to better understand the relationship of different solvents and solvent mixtures on the process map, as well as how changing solvent compositions during drying may influence the solidification pathway.

Finally, the process map has important implications for how to improve crystal coverage using process parameters. A common approach in the literature for increasing crystal coverage of a given solvent-solute system is to increase the substrate temperature or the convective drying air velocity, which effectively increases  $\beta$ . The process map suggests improvement of coverage if increasing  $\beta$  increases only Biwith no decrease in  $\Lambda$ . However, in reality, these effects are not so simple. For example, Hossain and co-workers showed that increasing  $\beta$  significantly decreases b (Hossain et al., 2023, publication in preparation, Supporting Information, Section S.12). More specifically, films of MAPbI<sub>3</sub> in GBL coated at 20 and 80 °C had  $Bi \approx 4 \times 10^{-5}$  and  $Bi \approx 1 \times 10^{-3}$ , respectively. However, in the case of MAPbI3 in GBL, a higher process temperature led to higher nucleation rates and smaller nuclei spacing, from  $b \approx 3 \ \mu \text{m}$  at 20 °C to  $b \approx 0.25 \ \mu \text{m}$  at 80 °C. Thus, increasing  $\beta$  by 2 orders of magnitude increased Biproportionally but decreased  $\Lambda^2$  by 2 orders of magnitude from  $\Lambda^2 \approx 1$  to  $\Lambda^2 \approx 8 \times 10^{-3}$ , such that  $Bi^*$  was unchanged. The constant Bi\* translated to no effective change in crystal coverage, as reported by the researchers. This result is most likely due to the retrograde solubility of MAPbI3 in GBL, which results in more nucleation with increasing temperature. Nevertheless, these results suggest that solvent choice largely predetermines the location on the process map and that process parameters have very little impact on significantly improving crystal coverage, but more work is needed to make a definitive conclusion. These results emphasize the importance of fundamental studies relating process parameters and b. Only then can we develop a quantitative understanding of whether and how process parameters can be used to control crystal coverage.

#### CONCLUSIONS

In most diffusion-driven solidification models, stable nuclei in thin films are assumed to grow from a semi-infinite medium such that subsequent growth is kinetically limited. 9,14,40-42 However, the assumption of growth into a semi-infinite medium is not relevant for thin films. This work presents a quasi-2D model to understand the effect of processing parameters on solid growth in thin films. The model assumes that the film is sufficiently thin such that diffusion in the horizontal direction is dominant and that evaporation dictates the height of the wet film. Nondimensionalization of the governing equations revealed two dimensionless groups: the modified Biot number, Bi\*, and the solidification Peclet number, Pe. The model results clearly show that the solid morphology and film coverage are predominately determined by the magnitude of Bi\*, which is a combination of the traditional Bi (i.e., process parameters) and  $\Lambda^2$  (i.e., nucleation

There are essentially three important regimes of  $Bi^*$ : high, low, and intermediate. At  $Bi^* < 1$ , the horizontal diffusion length scale quickly exceeds the separation distance between

neighboring nuclei, such that confinement leads to depletion, which significantly reduces thickness uniformity and connectivity between solid domains. Only when  $Bi^*\gg 1$  are the horizontal diffusion length scales small enough to prevent depletion, such that the substrate is uniformly coated. At intermediate modified Biot number, i.e.,  $Bi^*\approx 1$ , the coated film quality is sensitive to the value of Pe and can range from poorly coated to fully coated depending on the value of  $Bi^*$  and Pe. The model results are quantitatively validated via the coating and drying of perovskite thin films using three different solvent systems, with additional Bi values calculated for common solvents not examined in this study are given in the Supporting Information (see Table S1). The model and experiments are in good agreement.

Although our experimental case studies focused on perovskite photovoltaic films, the model results are presented in a generalized way so as to apply to arbitrary solute-solvent(s) systems, drying methods, and coating processes. A process map was constructed via the two fundamental dimensionless groups Bi and  $\Lambda$ . This representation shows two distinct regimes of poorly (<0.5 coverage) and fully (>0.99 coverage) connected coatings, and an intermediate transition regime where the coverage strongly depends on the value of Bi and  $\Lambda$ . Experimental results clearly showed that Bi and  $\Lambda$  are strongly coupled and are not easily manipulated independently. This fact has important implications for the ability to effectively control solid morphology and coverage via process parameters. Strategies for moving around the coating quality process map include achieving high evaporation rates, minimizing Pe, and increasing the aspect ratio  $\Lambda$  (as a function of process parameters like concentration, coating thickness, temperature, seeding, salt formulation, and solvent choice). However, more work is needed to measure and better understand the range of  $\Lambda$  achievable for a given solute-solvent choice. For now, we conclude that the solid morphology and coverage appear to be predefined by the choice of solute-solvent system. We look forward to the comparison of future experimental results to better understand the relationship between processing parameters and solid film morphology. Such experiments are the subject of ongoing research.

#### ASSOCIATED CONTENT

#### Supporting Information

The Supporting Information is available free of charge at https://pubs.acs.org/doi/10.1021/acs.langmuir.3c01469.

Derivations for the equations presented, detailed image analysis to calculate coverage, and tabulated values for sample calculations (PDF)

## AUTHOR INFORMATION

### **Corresponding Authors**

Nicolas J. Alvarez — Department of Chemical and Biological Engineering, Drexel University, Philadelphia, Pennsylvania 19104, United States; orcid.org/0000-0002-0976-6542; Email: alvarez@drexel.edu

Richard A. Cairncross — Department of Chemical and Biological Engineering, Drexel University, Philadelphia, Pennsylvania 19104, United States; Email: cairncross@drexel.edu

#### **Authors**

Jesse L. Starger — Department of Chemical and Biological Engineering, Drexel University, Philadelphia, Pennsylvania 19104, United States; orcid.org/0000-0002-2649-6281

Aaron T. Fafarman — Department of Chemical and Biological Engineering, Drexel University, Philadelphia, Pennsylvania 19104, United States; orcid.org/0000-0003-3652-3383

Jason B. Baxter — Department of Chemical and Biological Engineering, Drexel University, Philadelphia, Pennsylvania 19104, United States; orcid.org/0000-0001-8702-3915

Complete contact information is available at: https://pubs.acs.org/10.1021/acs.langmuir.3c01469

#### Note

The authors declare no competing financial interest.

#### ACKNOWLEDGMENTS

The authors thank Dr. Maimur Hossain for assistance with perovskite film coatings, Jacob Bolduc for assistance with AFM, and Taber Yim for assistance with SEM. Funding was provided by NSF Grant CMMI-1933819.

### NOMENCLATURE

```
x, position, m
x_{\text{xtal}} position at solid-liquid interface, m
\hat{x}, dimensionless position, —
\hat{x}_{\text{xtal}}, dimensionless position at solid-liquid interface, —
x_i, node position, -
b, domain width, —
h, film height, m
h_0, initial film height, m
h_{\text{xtal}}, height at solid-liquid interface, m
\hat{h}_{	ext{xtal}}, dimensionless height at solid—liquid interface, —
\hat{h}_0, initial dimensionless height, —
t, time, s
\tau_{\rm D,x}, characteristic lateral diffusion time scale, s
	au_{
m D,y}, characteristic vertical diffusion time scale, s
	au_{\rm evap}, evaporation time scale, s
D, diffusion coefficient, m^2 s<sup>-1</sup>
\hat{t}, dimensionless time, –
v, velocity, m/s
v_0, characteristic initial velocity, m/s
v_{i,x}, node velocity in x-direction, —
\hat{v}, dimensionless velocity (v/v_0), —
\hat{v}_{\text{xtal}}, dimensionless solid interface velocity, —
\hat{\nu}_0, initial dimensionless solid interface velocity, —
k_o, first-order rate constant, m/s
\phi_{	ext{S}}, solvent volume fraction, —
\phi_{	ext{A}\prime} solute volume fraction, —
\phi_{\rm A}^{0}, initial solute volume fraction, — \phi_{\rm A}^{\rm sat}, saturation solute volume fraction, —
Pe, Peclet number, -
Bi, traditional Biot number, —
Bi*, modified Biot number, —
\Lambda, wet film aspect ratio, –
E_{SV}, evaporative volume flux, m<sup>3</sup>/m<sup>2</sup>/s
\beta, mass transfer coefficient, m/s
\alpha_{\rm S}, solvent liquid-vapor expansion coefficient, —
p_{\text{vap}}, solvent vapor pressure, Pa
R, gas constant, m^3 Pa K^{-1} mol<sup>-1</sup>
T, temperature, K
V_A, solute molar volume, m<sup>3</sup>/mol
```

 $\overline{V}_{\rm S}$ , solvent molar volume, m<sup>3</sup>/mol i, node number, —  $\zeta_{i\prime}$ , fractional node position, — N, total nodes in domain, —  $\varepsilon_{\rm rel}$ , relative tolerance, —  $\varepsilon_{\rm abs\prime}$  absolute tolerance, —

#### REFERENCES

- (1) LaMer, V. K.; Dinegar, R. H. Theory, Production and Mechanism of Formation of Monodispersed Hydrosols. *J. Am. Chem. Soc.* **1950**, 72, 4847–4854.
- (2) Avrami, M. Kinetics of Phase Change. I General Theory. J. Chem. Phys. 1939, 7, 1103–1112.
- (3) Avrami, M. Kinetics of Phase Change. II Transformation-Time Relations for Random Distribution of Nuclei. *J. Chem. Phys.* **1940**, *8*, 212–224.
- (4) Avrami, M. Granulation, Phase Change, and Microstructure Kinetics of Phase Change. III. *J. Chem. Phys.* **1941**, *9*, 177–184.
- (5) Volmer, M. Thermodynamische Folgerungen ans der Zustandsgleichung für adsorbierte Stoffe. Z. Phys. Chem. 1925, 115U, 253–260.
- (6) Volmer, M.; Weber, A. Keimbildung in übersättigten Gebilden. Z. Phys. Chem. 1926, 119U, 277–301.
- (7) Gilbert, E. N. Random Subdivisions of Space into Crystals. *The Annals of Mathematical Statistics*; Institute of Mathematical Statistics, 1962; Vol. 33; pp 958–972.
- (8) Whitehead, C. B.; Özkar, S.; Finke, R. G. LaMer's 1950 Model for Particle Formation of Instantaneous Nucleation and Diffusion-Controlled Growth: A Historical Look at the Model's Origins, Assumptions, Equations, and Underlying Sulfur Sol Formation Kinetics Data. Chem. Mater. 2019, 31, 7116–7132.
- (9) Dunlap-Shohl, W. A.; Zhou, Y.; Padture, N. P.; Mitzi, D. B. Synthetic Approaches for Halide Perovskite Thin Films. *Chem. Rev.* **2019**, *119*, 3193–3295.
- (10) Deng, Y.; Peng, E.; Shao, Y.; Xiao, Z.; Dong, Q.; Huang, J. Scalable fabrication of efficient organolead trihalide perovskite solar cells with doctor-bladed active layers. *Energy Environ. Sci.* **2015**, 8, 1544–1550.
- (11) Angmo, D.; DeLuca, G.; Scully, A. D.; Chesman, A. S.; Seeber, A.; Zuo, C.; Vak, D.; Bach, U.; Gao, M. A Lab-to-Fab Study toward Roll-to-Roll Fabrication of Reproducible Perovskite Solar Cells under Ambient Room Conditions. *Cell Rep. Phys. Sci.* **2021**, *2*, 100293.
- (12) Zhou, Y.; Game, O. S.; Pang, S.; Padture, N. P. Microstructures of Organometal Trihalide Perovskites for Solar Cells: Their Evolution from Solutions and Characterization. *J. Phys. Chem. Lett.* **2015**, *6*, 4827–4839.
- (13) Zhou, Y.; Herz, L. M.; Jen, A. K.-Y.; Saliba, M. Advances and challenges in understanding the microscopic structure—property—performance relationship in perovskite solar cells. *Nat. Energy* **2022**, *7*, 794–807.
- (14) Rahaman, M. N. Ceramic Processing and Sintering, 2nd ed.; Materials Engineering; M., Dekker, Ed.; Marcel Dekker Inc.: New York, 2003.
- (15) Beers, K. L.; Douglas, J. F.; Amis, E. J.; Karim, A. Combinatorial Measurements of Crystallization Growth Rate and Morphology in Thin Films of Isotactic Polystyrene. *Langmuir* **2003**, *19*, 3935–3940.
- (16) Deegan, R. D.; Bakajin, O.; Dupont, T. F.; Huber, G.; Nagel, S. R.; Witten, T. A. Capillary flow as the cause of ring stains from dried liquid drops. *Nature* **1997**, *389*, 827–829.
- (17) Deegan, R. D.; Bakajin, O.; Dupont, T. F.; Huber, G.; Nagel, S. R.; Witten, T. A. Contact line deposits in an evaporating drop. *Phys. Rev. E* **2000**, *62*, 756–765.
- (18) Ahmadian-Yazdi, M.-R.; Eslamian, M. Effect of Marangoni Convection on the Perovskite Thin Liquid Film Deposition. *Langmuir* **2021**, *37*, 2596–2606.
- (19) Cussler, E. L. Diffusion: Mass Transfer in Fluid Systems, 3rd ed.; Cambridge University Press: Cambridge, New York, 2009; p 226389413.

- (20) Ternes, S.; Börnhorst, T.; Schwenzer, J. A.; Hossain, I. M.; Abzieher, T.; Mehlmann, W.; Lemmer, U.; Scharfer, P.; Schabel, W.; Richards, B. S.; Paetzold, U. W. Drying Dynamics of Solution-Processed Perovskite Thin-Film Photovoltaics: In Situ Characterization, Modeling, and Process Control. *Adv. Energy Mater.* **2019**, *9*, 1901581.
- (21) Bird, R. B.; Stewart, W. E.; Lightfoot, E. N. Transport Phenomena; Wiley: New York, 2007.
- (22) Ternes, S.; Mohacsi, J.; Lüdtke, N.; Pham, H. M.; Arslan, M.; Scharfer, P.; Schabel, W.; Richards, B. S.; Paetzold, U. W. Drying and Coating of Perovskite Thin Films: How to Control the Thin Film Morphology in Scalable Dynamic Coating Systems. *ACS Appl. Mater. Interfaces* **2022**, *14*, 11300–11312.
- (23) De Yoreo, J. J.; Gilbert, P. U. P. A.; Sommerdijk, N. A. J. M.; Penn, R. L.; Whitelam, S.; Joester, D.; Zhang, H.; Rimer, J. D.; Navrotsky, A.; Banfield, J. F.; Wallace, A. F.; Michel, F. M.; Meldrum, F. C.; Colfen, H.; Dove, P. M. Crystallization by particle attachment in synthetic, biogenic, and geologic environments. *Science* **2015**, 349, 3296760
- (24) Fateev, S. A.; Petrov, A. A.; Khrustalev, V. N.; Dorovatovskii, P. V.; Zubavichus, Y. V.; Goodilin, E. A.; Tarasov, A. B. Solution Processing of Methylammonium Lead Iodide Perovskite from  $\gamma$ -Butyrolactone: Crystallization Mediated by Solvation Equilibrium. *Chem. Mater.* **2018**, *30*, 5237–5244.
- (25) The MathWorks. MATLAB Mathematics, 2022; p 708.
- (26) Huang, W.; Ren, Y.; Russell, R. D. Moving Mesh Methods Based on Moving Mesh Partial Differential Equations. *J. Comput. Phys.* **1994**, *113*, 279–290.
- (27) Schmidt-Hansberg, B.; Baunach, M.; Krenn, J.; Walheim, S.; Lemmer, U.; Scharfer, P.; Schabel, W. Spatially resolved drying kinetics of multi-component solution cast films for organic electronics. *Chem. Eng. Process.: Process Intensif.* **2011**, *50*, 509–515.
- (28) Mullin, J. W. *Crystallization*, 4th ed.; Butterworth-Heinemann: Oxford; Boston, 2001.
- (29) Toldy, A. I.; Badruddoza, A. Z. M.; Zheng, L.; Hatton, T. A.; Gunawan, R.; Rajagopalan, R.; Khan, S. A. Spherical Crystallization of Glycine from Monodisperse Microfluidic Emulsions. *Cryst. Growth Des.* **2012**, *12*, 3977–3982.
- (30) Pettit, D.; Fontana, P. Comparison of sodium chloride hopper cubes grown under microgravity and terrestrial conditions. *npj Microgravity* **2019**, *5*, 25.
- (31) Ni, J.; Beckermann, C. A volume-averaged two-phase model for transport phenomena during solidification. *Metall. Trans. B* **1991**, *22*, 349–361.
- (32) Samanta, D.; Zabaras, N. Modelling convection in solidification processes using stabilized finite element techniques. *Int. J. Numer. Methods Eng.* **2005**, *64*, 1769–1799.
- (33) Chen, T.; Zhou, Y.; Rafailovich, M. Application of Machine Learning in Perovskite Solar Cell Crystal Size Distribution Analysis. *MRS Adv.* **2019**, *4*, 793–800.
- (34) Hamill, J. C.; Schwartz, J.; Loo, Y.-L. Influence of Solvent Coordination on Hybrid Organic–Inorganic Perovskite Formation. *ACS Energy Lett.* **2018**, *3*, 92–97.
- (35) Hamill, J. C.; Romiluyi, O.; Thomas, S. A.; Cetola, J.; Schwartz, J.; Toney, M. F.; Clancy, P.; Loo, Y.-L. Sulfur-Donor Solvents Strongly Coordinate Pb<sup>2+</sup> in Hybrid Organic–Inorganic Perovskite Precursor Solutions. *J. Phys. Chem. C* **2020**, *124*, 14496–14502.
- (36) Deng, Y.; Van Brackle, C. H.; Dai, X.; Zhao, J.; Chen, B.; Huang, J. Tailoring solvent coordination for high-speed, room-temperature blading of perovskite photovoltaic films. *Sci. Adv.* **2019**, *S*, No. eaax7537.
- (37) Stevenson, J.; Sorenson, B.; Subramaniam, V. H.; Raiford, J.; Khlyabich, P. P.; Loo, Y.-L.; Clancy, P. Mayer Bond Order as a Metric of Complexation Effectiveness in Lead Halide Perovskite Solutions. *Chem. Mater.* **2017**, *29*, 2435–2444.
- (38) Konstantakou, M.; Perganti, D.; Falaras, P.; Stergiopoulos, T. Anti-Solvent Crystallization Strategies for Highly Efficient Perovskite Solar Cells. *Crystals* **2017**, *7*, 291.

- (39) Tavakoli, M. M.; Yadav, P.; Prochowicz, D.; Sponseller, M.; Osherov, A.; Bulović, V.; Kong, J. Controllable Perovskite Crystallization via Antisolvent Technique Using Chloride Additives for Highly Efficient Planar Perovskite Solar Cells. *Adv. Energy Mater.* **2019**, *9*, 1803587.
- (40) He, M.; Li, B.; Cui, X.; Jiang, B.; He, Y.; Chen, Y.; O'Neil, D.; Szymanski, P.; EI-Sayed, M. A.; Huang, J.; Lin, Z. Meniscus-assisted solution printing of large-grained perovskite films for high-efficiency solar cells. *Nat. Commun.* **2017**, *8*, 16045.
- (41) Hu, H.; Singh, M.; Wan, X.; Tang, J.; Chu, C.-W.; Li, G. Nucleation and crystal growth control for scalable solution-processed organic—inorganic hybrid perovskite solar cells. *J. Mater. Chem. A* **2020**, *8*, 1578–1603.
- (42) Park, S. J.; Kim, A. R.; Hong, J. T.; Park, J. Y.; Lee, S.; Ahn, Y. H. Crystallization Kinetics of Lead Halide Perovskite Film Monitored by In Situ Terahertz Spectroscopy. *J. Phys. Chem. Lett.* **2017**, *8*, 401–406.